

Influence of nonequilibrium quasiparticles in phonon imaging of superconductors: Consistency with BCS theory in Pb crystals

T. L. Head* and J. P. Wolfe

Physics Department and Frederick Seitz Materials Research Laboratory, University of Illinois at Urbana-Champaign,
1110 West Green Street, Urbana, Illinois 61801, USA

(Received 28 November 2007; revised manuscript received 16 July 2008; published 22 August 2008)

This paper is the second part of a study motivated by the prediction of Overhauser and Daemen [A. W. Overhauser and L. L. Daemen, *Phys. Rev. Lett.* **61**, 1885 (1988)] that the electronic ground state of Pb exhibits a spin-density wave (SDW) that leads to a highly anisotropic superconducting gap. The first part of our study [J. D. Short, T. L. Head, and J. P. Wolfe, *Phys. Rev. B* **78**, 054515 (2008)] extended the theoretical predictions to the actual Fermi surface of Pb and initiated phonon imaging experiments on high purity Pb. The temperature dependence of the phonon absorption by quasiparticles over a 1.45–2.1 K temperature range was found to be much weaker than the $\exp(-\Delta_o/k_B T)$ form using the generally accepted gap parameter $\Delta_o=1.35$ meV for Pb. In addition, the absorption coefficients obtained for two crystals of different thickness were not consistent with phonon absorption by quasiparticles in thermal equilibrium with the lattice. To explain these two anomalies in the context of the BCS theory of superconductivity, we examine the possible effects of nonequilibrium quasiparticles generated by the laser source and bolometer detector. Detailed experiments varying crystal length, source size, excitation power, and pulse duration over wide limits enable us to isolate the phonon absorption by both nonequilibrium and thermal-equilibrium quasiparticles. The wide variety of data yields an equilibrium quasiparticle density that varies as $\exp(-\Delta/k_B T)$ with $\Delta=1.32 \pm 0.07$ meV, in good agreement with BCS theory with $\Delta_o=1.35$ meV, and inconsistent with the electronic-specific-heat data of van der Hoeven and Keesom [B. J. C. van der Hoeven, Jr. and P. Keesom, *Phys. Rev.* **137**, 103 (1965)] that motivated the SDW hypothesis in Pb. In summary, the highly anisotropic absorption of ballistic phonons in superconducting Pb provides a unique measure of equilibrium quasiparticle density that agrees with BCS theory extending to $\exp(-\Delta/k_B T)=2.6 \times 10^{-5}$ at 1.45 K.

DOI: [10.1103/PhysRevB.78.054516](https://doi.org/10.1103/PhysRevB.78.054516)

PACS number(s): 74.25.Ld, 74.25.Jb, 72.10.Di, 75.30.Fv

I. OVERVIEW

The concept that the electronic ground state of a metal can support a spin-density wave (SDW) is quite remarkable and has been convincingly demonstrated¹ for the *d*-band electronic ground state of Cr, where the SDW wavelength is incommensurate with the lattice period. Overhauser² proposed that even metals with *s*-wave ground states can exhibit an SDW. Overhauser and Daemen^{3,4} calculated the effect of SDWs on superconductivity in Pb, motivated by anomalous specific-heat data reported by van der Hoeven and Keesom^{5,6} shown in Fig. 1.

According to Ref. 3, an SDW ground state in Pb would produce a highly anisotropic superconducting gap, $\Delta(\mathbf{k})$, characterized by deep valleys where commensurate SDW wave vectors roughly match $2k_{\text{Fermi}}$. The long tail in the specific heat was attributed to quasiparticles in the SDW valleys. In Sec. III in this paper and Sec. IV of Ref. 7 (referred to as Paper I), we discuss these and other experiments cited as evidence for SDWs in Pb.⁸

Our experiments use high frequency ballistic phonons as an internal probe of superconducting Pb. Phonons with energies below the superconducting gap energy can travel ballistically across millimeter-sized crystals of pure Pb, occasionally scattering from thermally excited quasiparticles. We showed in Paper I that the shape of the Fermi surface in Pb greatly amplifies the phonon-quasiparticle scattering for phonon wave vectors in the $\{111\}$ planes of the crystal. The phonon images clearly exhibit sharp lines of reduced phonon

intensity due to phonon absorption by quasiparticles.

The first experiments seemed to support the idea of reduced-gap regions by indicating a relatively weak temperature dependence of quasiparticle density over our 1.4–2.1 K experimental range; however, crystals of different thicknesses showed an unexpected dependence of phonon absorption coefficient, α , on path length. A detailed model of quasiparticles scattered within SDW valleys, as well as quasiparticles ejected from the valleys, did not satisfactorily account for the variations of phonon absorption with temperature and path length (i.e., *crystal thickness L*). Furthermore, a low-pass phonon filter experiment did not support the idea that the absorbed phonons eject quasiparticles from deep valleys in the gap.

Our analysis in Paper I assumed that the density of quasiparticles in the phonon-imaging experiments followed the $\exp(-\Delta/k_B T)$ form expected for quasiparticles in thermal equilibrium with the lattice at temperature *T* well below *T_c*. This was a natural first assumption for quasiparticles in the bulk of our millimeter-sized crystals that were immersed in a superfluid helium bath. The variability of the fitted gap parameter Δ with path length *L*, however, suggests a spatially varying density of quasiparticles in the crystal. In this paper, we allow for the role of such nonequilibrium effects.

II. ACCOUNTING FOR NONEQUILIBRIUM QUASIPARTICLES

Nonequilibrium quasiparticles can enter a phonon-imaging experiment from two sources: the excitation point

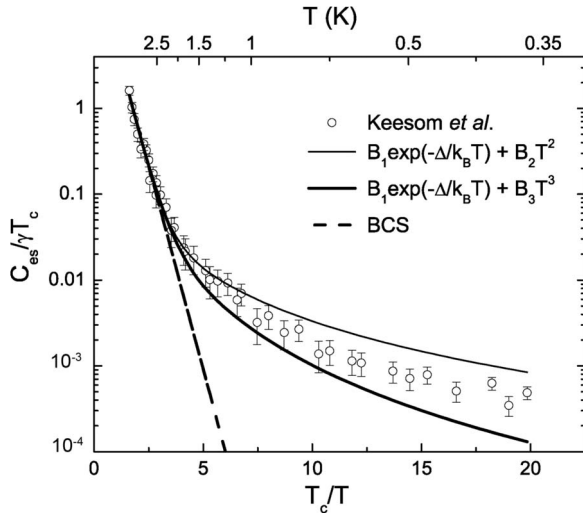


FIG. 1. Apparent low-temperature superconducting electronic specific heat of Pb divided by γT_c , where T_c is 7.19 K for high-purity Pb, from Ref. 5. The C_{es} data were obtained by subtracting a fit to the total normal-state specific heat at a magnetic field $H > H_c$ from the total superconducting-state specific heat at zero magnetic field and adding γT , the term that corresponds to the normal-state electronic contribution. The line labeled BCS has the form $B_1 \exp(-\Delta/k_B T)$ with $B_1=48.5$ and $\Delta=1.35$ meV. Empirical fits to the low temperature tail are discussed in Sec. III.

and the superconducting bolometer detector. Laser excitation of the normal-metal film deposited on the crystal produces a Planckian source of phonons.^{7,9,10} The Pb crystal is hotter near the point source, causing a small region with higher quasiparticle density than in the bulk of the crystal. Also, to operate experiments over a range of temperatures below the critical temperature of the detector, it is necessary to raise the temperature of the detector film to its critical temperature by increasing its bias current. This second source of nonequilibrium quasiparticles (near the detector) is unavoidable in the variable temperature experiments essential to this study.

Because we are interested in the *equilibrium* properties of Pb, we wish to minimize the number of *nonequilibrium* quasiparticles created as a by-product of the phonon-imaging technique. The phonon-source temperature decreases with the fourth root of the incident power, so simply lowering the power of the laser pulse reduces the source temperature very little. However, a combination of increasing both the pulse length, detection time, and source area while lowering the laser power results in a usable dynamic range of about 5000 in power density, allowing us to significantly reduce the phonon source temperature and hence the effects of nonequilibrium quasiparticles.

Our experiments divide into two categories depending on excitation-pulse length. First, short-pulse (10 ns) experiments at high to medium excitation powers, and second, long-pulse experiments (250–1000 ns) that allow operation at low excitation powers with the use of longer averaging times. The energy per pulse (hence signal-to-noise) can be similar in both short- and long-pulse cases, but because the latter case produces a lower temperature phonon source, a smaller number of nonequilibrium quasiparticles are created.

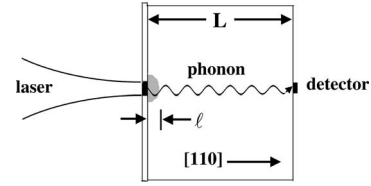


FIG. 2. The transmission of ballistic phonons from the laser-heated film through two regions in the Pb crystal. A small region of dimension ℓ has an elevated local temperature and higher (“non-equilibrium”) quasiparticle density. The bulk crystal with thickness $L \gg \ell$ has a thermal-equilibrium density of quasiparticles. A non-equilibrium region near the detector is not shown, but the parameter $\beta\ell$ described in the text incorporates the effects of both heated regions. A typical laser spot of $15 \mu\text{m}$ ($50 \mu\text{m}$) is used for high (low) power experiments.

The laser beam heats a region on the Au excitation film, which has been evaporated directly onto the Pb crystal.¹¹ A small region of dimension ℓ adjacent to the heated film is raised to a higher temperature than that of the bulk crystal, which is at the bath temperature. The heated Pb region has a higher density of quasiparticles, which we designate as nonequilibrium quasiparticles. Phonons from the heated source propagate ballistically to the detector along the $[110]$ direction, passing through both heated and bulk regions of the crystal. A schematic diagram of these ideas is shown in Fig. 2.

We have no direct measure of the size ℓ of the heated region or its effective temperature, but the fraction of transmitted phonons through this region equals $\exp(-\beta\ell)$, where β is an average absorption coefficient proportional to an average quasiparticle density. We use $\beta\ell$ as an adjustable fitting parameter characterizing the effect of nonequilibrium quasiparticles in a given experiment. The intensity of phonons reaching the detector along the $[110]$ direction (corresponding to the laser position x_o) is given by:

$$I(x_o) = I_o e^{-\beta\ell} e^{-\alpha L}, \quad (1)$$

where α is the *equilibrium* phonon absorption coefficient in the bulk crystal, and we have assumed that the crystal thickness L is much greater than the size of the heated region ℓ . I_o represents the intensity of ballistic phonons arriving along the $[110]$ direction in the absence of quasiparticle absorption, which we cannot directly measure. Any effect due to crystal heating near the detector is also incorporated in the parameter $\beta\ell$.

An alternate scenario views the Planckian phonons emitted from the film directly creating nonequilibrium quasiparticles near the surface of the crystal. A typical phonon has energy considerably larger than the superconducting gap (see Fig. 5 in Paper I), creating a high-energy quasiparticle that quickly relaxes back to the gap edge by acoustic phonon emission. These nonequilibrium quasiparticles form a diffuse cloud surrounding the excitation point. If $\beta(x)$ represents the local absorption coefficient for phonons, the probability that a ballistic phonon traverses the cloud without being absorbed is again $\exp(-\beta\ell)$ with $\beta\ell \equiv \int \beta(x) dx$, integrated along $[110]$ through the cloud. Both viewpoints yield a single parameter

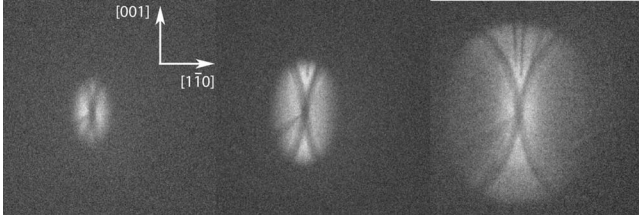


FIG. 3. Three images of ballistic phonon intensity measured at $T=2$ K with increasing gate widths starting at the $[110]$ ballistic time: $\Delta t=50, 200,$ and 500 ns for a crystal thickness of $L=4$ mm. The phonons traveling at angles outside the bright “circles” have ballistic propagation times outside the selected temporal gate width and are therefore not recorded in the image, or in a standard line scan through the center of the image. For the experiments in this paper, the cylindrical crystal is oriented so that the raster scan coincides with the crystalline axes shown. The dark “X” is due to phonon absorption by quasiparticles. Other dark features in this particular experiment arise from regions of poor film adhesion or near-surface defects.

characterizing phonon absorption due to nonequilibrium quasiparticles. Notice that the exact form of $\beta(x)$ is not important in our analysis as long as it is only weakly dependent on crystal temperature. Although we must account for nonequilibrium quasiparticles, it is the bulk absorption coefficient $\alpha(T)$ —driven by thermal excitations—that we wish to determine because of its direct relationship to the superconducting gap minimum.

III. PHONON ABSORPTION BY QUASIPARTICLES AT LOW EXCITATION POWER

In this section, we describe experiments designed to minimize the effect of nonequilibrium quasiparticles. The key is to reduce the power density (power per area) of the excitation region and simultaneously broaden the pulse length. The broader pulse length ($0.45 \mu\text{s}$ for a 1.26 mm sample) and a comparable boxcar sampling gate Δt permit better signal averaging. Using this experimental configuration, we measure the time-integrated flux of the longitudinal acoustic (LA) phonons while excluding transverse acoustic (TA) phonons.

The effect of the boxcar sampling gate is demonstrated in Fig. 3, using a short excitation pulse. This is a series of phonon images at increasing boxcar gate width following a 10 -ns laser pulse. As in Paper I, the quasiparticle absorption “X” is clearly seen, its center corresponding to the $[110]$ propagation direction. As the boxcar gate width is increased, ballistic phonons with larger source-to-detector distances (hence longer time-of-flights) are observed. A cutoff in phonon intensity occurs when the time-of-flight (path-length/sound velocity) is longer than the end of the boxcar collection gate $t_g + \Delta t$, where t_g designates the beginning of the gate and Δt is the gate width. The signals are primarily due to ballistic phonons because scattered phonons have significantly delayed arrival times.

Figure 4(a) shows a Monte Carlo simulation of LA phonons traveling ballistically from a point source. This time-integrated intensity pattern shows the effect of phonon

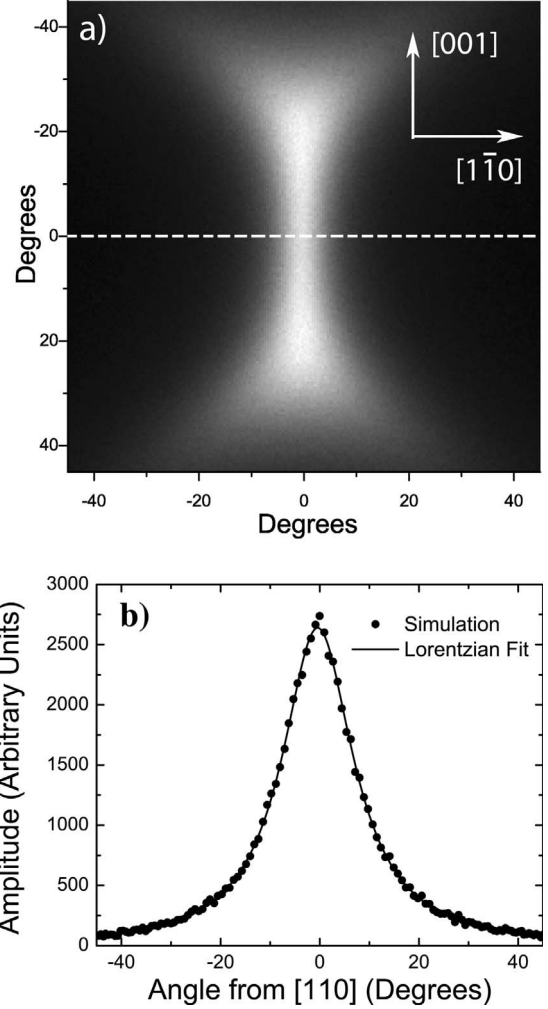


FIG. 4. (a) A Monte Carlo simulation of ballistic LA phonons transmitted through Pb, using the known elastic constants and density. (b) A profile taken along the dashed line shown in part (a). The profile fits extremely well to a Lorentzian function with a spatial width determined by the sample length.

focusing.⁹ Our standard line scan through the center of this distribution is plotted as the dots in Fig. 4(b). We find that this “ballistic” profile is well represented by the Lorentzian function,

$$I_b(x) = \frac{I_o w_b^2}{[4(x - x_o)^2 + w_b^2]}, \quad (2)$$

where I_o is the peak intensity and w_b is the full-width at half-maximum of the distribution.

The spatial distribution of absorbed phonons was calculated in Paper I by considering their kinetics with quasiparticles on the standard Fermi surface of Pb. The shape of this distribution depends on the shape of the Fermi surface. The observed experimental distribution also depends on spatial resolution, phonon source size, and possibly crystal temperature. As in Paper I, we approximate the fraction of absorbed phonons by a Gaussian function with width σ_a :

$$A(x) = A_o e^{[-(x - x_o)^2 / 2\sigma_a^2]}, \quad (3)$$

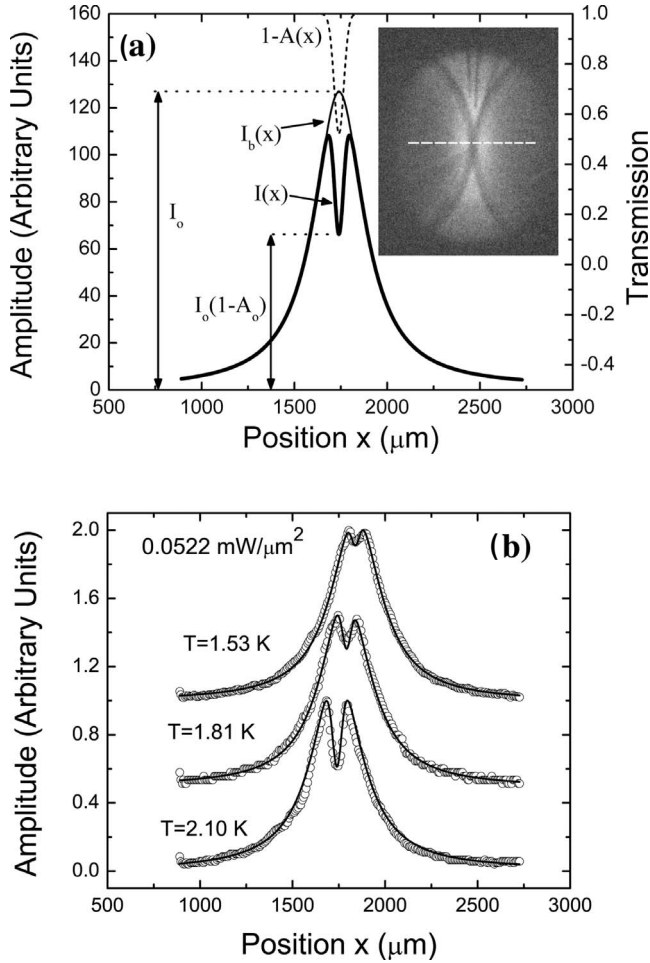


FIG. 5. (a) Theoretical curves of ballistic intensity $I_b(x)$, transmitted fraction $1-A(x)$, and resulting transmitted intensity $I(x)$, all plotted for the scan line in a (110) plane shown as the dashed line in the phonon image (inset). $I_b(x)$ is a Lorentzian that matches the theoretical line shape and $A(x)$ is an empirical Gaussian function. (b) Experimental line scans for a 1.26-mm crystal fitted to $I(x) = I_b(x)[1-A(x)]$. This experiment uses a long pulse length of $0.45 \mu\text{s}$, a boxcar-gate width of $0.46 \mu\text{s}$, and the excitation density shown. The slight horizontal shift in the profiles arises from a sample displacement as the cryostat pressure is lowered.

where A_o is the *fractional absorption* along the [110] direction.

Considering that the *fraction of transmitted ballistic phonons* is $[1-A(x)]$, the theoretical profile of transmitted phonons in Pb is given by:

$$I(x) = I_b(x)[1 - A(x)], \quad (4)$$

which is plotted as the heavy solid curve in Fig. 5(a). The adjustable parameters in this function are the amplitudes I_o and A_o , the widths w_b and σ_a , and the central position x_o .

Figure 5(b) shows a fit of this function to the experimental data for our 1.26-mm crystal at three bath temperatures. Notice the large decrease in phonon absorption as the temperature is lowered from 2.10 to 1.53 K. Also notice the excellent fits of the Lorentzian function to the data. The Lorentzian width, $w_b = 323 \mu\text{m}$, is 15% narrower than that obtained by

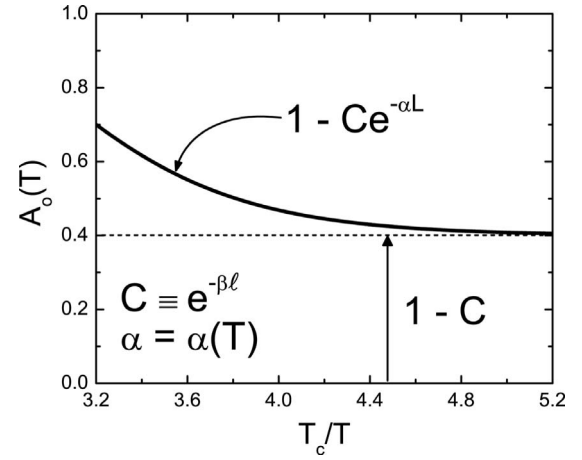


FIG. 6. Schematic illustration of the temperature dependence of the fractional absorption of phonons due to nonequilibrium phonons. The solid line represents Eq. (5), assuming a temperature-independent contribution from nonequilibrium quasiparticles and the BCS form of $\alpha(T)$.

fitting Eq. (2) to the Monte Carlo distribution of Fig. 4. We will use the experimental value of w_b , appropriately scaled to crystal thickness, in the fitting function $I_b(x)$ for all analyses in this paper; i.e., it is no longer an adjustable parameter.

Despite the long pulse length and sampling times, the spatial profiles shown in Fig. 5(b) have little contribution from phonons scattered by mass defects in the bulk of the crystal. In Appendix A we calculate the expected spatial profile for elastic scattering of phonons from isotopes of Pb, a process introduced in Paper I. A Gaussian-like distribution with a width considerably wider than the ballistic Lorentzian distribution is predicted. If we include this simulated profile, allowing its amplitude to be an adjustable parameter in the fit, the program chooses essentially zero scattering amplitude. A physical explanation for this result is given in Appendix A.

From Eqs. (1) and (4), the fractional transmission of phonons is given by $I(x_o)/I_o = 1 - A_o(T) = \exp(-\beta\ell - \alpha L)$. Assuming the low temperature ($T \ll T_c$) BCS form for the absorption coefficient,¹² $\alpha = 2\alpha_n e^{-\Delta/k_B T}$, we fit the absorption data to the function

$$A_o(T) = 1 - \exp(-\beta\ell - 2\alpha_n L e^{-\Delta/k_B T}), \quad (5)$$

where α_n is the absorption coefficient for the normal (non-superconducting) state and is assumed to be constant over our small temperature range.¹³ The physical interpretation of this equation is illustrated in Fig. 6. At low temperature, absorption due to nonequilibrium quasiparticles is dominant, $A_o \approx 1 - e^{-\beta\ell}$. As the bath temperature is raised, the contribution from equilibrium quasiparticles increases the fraction of absorbed phonons.

Figure 7(a) is a graph of the measured $A_o(T)$ for three different power densities. For each bath temperature T , the absorbed fraction A_o is determined from a fit of Eq. (4) to the experimental profile [Fig. 5(b)]. Equation (5) is used to fit these temperature dependence data with three adjustable parameters: $\beta\ell$, α_n , and Δ . When all three are allowed to vary

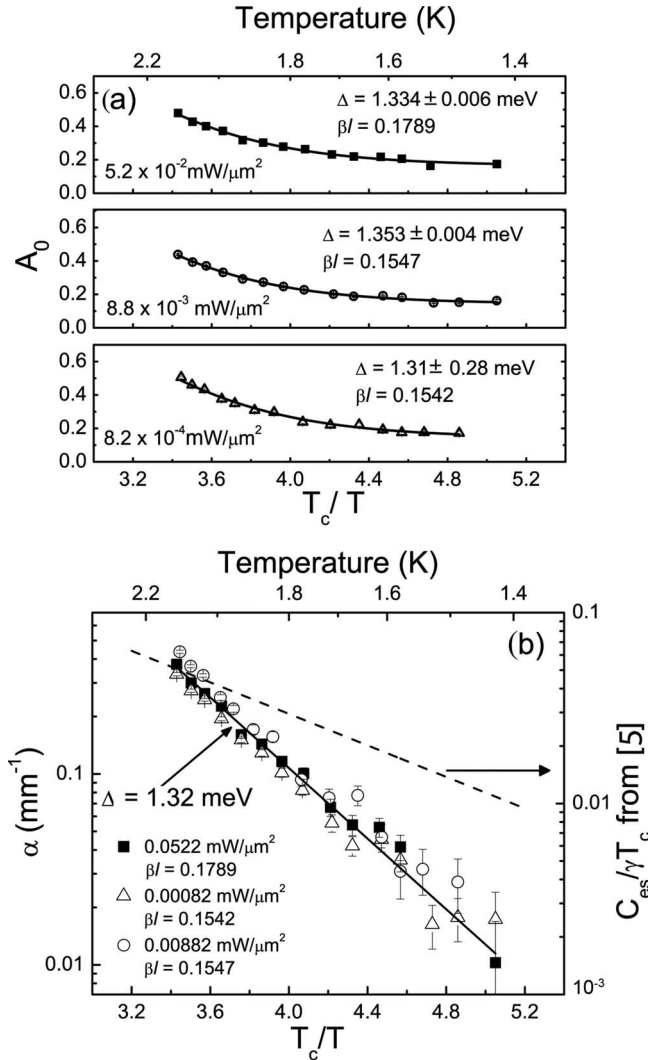


FIG. 7. (a) Plots for three different peak power densities of $A_o(T) = 1 - I(x_o)/I_o$ as a function of T_c/T , where $T_c = 7.19$ K is the superconducting transition of Pb. Notice that at larger values of T_c/T , the curves approach the constant $1 - e^{-\beta l}$, indicating the dominance of nonequilibrium quasiparticles. At lower T_c/T , $e^{-\alpha l}$ becomes important due to contributions from equilibrium quasiparticles in the bulk crystal. (b) Equilibrium absorption coefficient $\alpha(T)$ for the three data sets from part (a) match when the contribution of nonequilibrium quasiparticles is taken into account. The dashed line represents an exponential fit (yielding $\Delta = 0.6$ meV) to the superconducting electronic specific heat of Ref. 5, over the temperature range of our phonon imaging experiments.

in the analysis of $A_o(T)$ for a given power density, the fitted values Δ and βl are found to be quite insensitive to the fitted value of α_n ; therefore, we fix α_n at a median value of 293 mm^{-1} for these and all similar analyses in this paper. Theoretically it is reasonable that α_n is relatively independent of T because it represents a normal-state absorption constant. As seen in Fig. 7(a), excellent fits are obtained and the best-fit values of Δ and βl are listed.

Figure 7(b) is a semi-log graph of absorption coefficient α vs T_c/T for the three runs at different excitation power densities. All three show excellent agreement in magnitude and temperature dependence. The solid line through the data

yields a superconducting gap $\Delta = 1.32 \pm 0.05$ meV, consistent with the gaps determined individually by fitting $A_o(T)$, and close to the low temperature value $\Delta_o = 1.35$ meV measured by electron tunneling.^{14,15}

We regard this analysis of the phonon scattering by quasiparticles—obtained by minimizing the effects of nonequilibrium phonons with low excitation level—as strong support for the conventional gap in Pb. In contrast, the dashed line in Fig. 7(b) is an exponential fit over our 1.4–2.1 K temperature range to the electronic specific heat reported in Ref. 5 and shown in our Fig. 1. The specific-heat data would correspond to a factor of about five change in density of quasiparticles over this temperature range, compared to a factor of about 35 change obtained in the phonon-imaging experiments.

This large discrepancy between our results and the specific-heat experiments of Ref. 5 may be explained in a conference paper by Phillips *et al.*¹⁶ In the Discussion 19 addenda to this paper, Keesom showed that it was the *normal specific heat* (C_n) in his original data that changed with the addition of indium impurities, not the *superconducting specific heat* (C_s). For his undoped crystal, both C_s and C_n data showed linear dependences but with different slopes when plotted as C/T vs T^2 . (The data of Phillips *et al.*¹⁶ show no such anomaly for their undoped Pb crystal.) This unexpected deviation leads to a dependence between T^2 and T^3 for $C_{es} \equiv C_s - C_n + \gamma T$, which is *apparently unrelated to quasiparticle density*. The cause of the different slopes for C_n and C_s (vs T^2) in the undoped sample of Keesom *et al.*¹⁷ is unknown.

IV. TIME-RESOLVED PHONON ABSORPTION BY QUASIPARTICLES AT HIGH EXCITATION POWERS

Next we consider the same 1.26-mm crystal at considerably higher excitation levels, corresponding to higher source temperatures and phonon frequencies. The conditions are similar to those used in Paper I,¹⁰ but now nonequilibrium quasiparticles play a greater role. Moreover, we must take a more general approach in analyzing the spatial distributions because the observation times (boxcar gate widths) are relatively small and centered around the temporal peak of the ballistic signal. In this case, the ballistic spatial profiles, $I_b(x)$, are not simply the time-integrated Lorentzian form of Eq. (2).

Figure 8(a) shows a time trace of the transmitted ballistic phonons traveling along [110] following a 10-ns laser pulse. The pulse starts at the ballistic time-of-flight across the crystal and continues for a time characteristic of the source cooling. We know that these are ballistic phonons because sharp absorption dips are present in spatial profiles taken with a 10-ns gate positioned anywhere in the time trace.

Assume that energy E is deposited by the optical excitation and that this energy is released over time in the form of phonons. The phonon source radiates an instantaneous power $P(t)$ starting at $t=0$, such that $\int_0^\infty P(t) dt = E$. For an elastically isotropic solid and no phonon scattering, the phonon flux (power per area) at a distance r from the source at time t would be

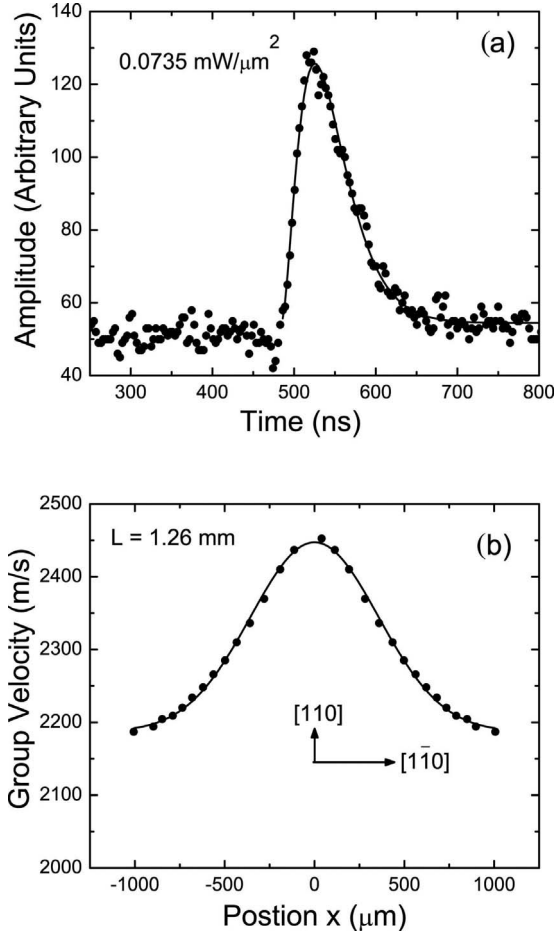


FIG. 8. (a) Ballistic heat pulse for a crystal of length $L = 1.26$ mm and peak power density 0.074 mW/ μm^2 . The solid curve is the function $P(t)$ described in the text and used in Eq. (8) to determine the ballistic spatial profile $I_b(x)$. (b) Dots are the calculated group velocities $v(x)$ for the position x on the scan line of the 1.26-mm crystal. Solid curve is a (Gaussian+constant) function used for $v(x)$ in Eq. (8).

$$\begin{aligned} \Phi(\mathbf{r}, t) &= 0 \quad \text{for } t < t_b, \\ &= \frac{P(t - t_b)}{4\pi r^2} \hat{\mathbf{r}} \quad \text{for } t \geq t_b, \end{aligned} \quad (6)$$

where $t_b = r/v$ is the ballistic time of flight with phonon velocity v , and $\hat{\mathbf{r}}$ is the unit vector along the radius r . Now consider a point at $r = (L^2 + x^2)^{1/2}$ on our standard scan line for a crystal of thickness L . The detector has an area $d_x d_y$ on a surface with normal $\hat{\mathbf{n}}$. For Pb we must include the (Lorentzian-like) phonon focusing factor $L(x)$, which incorporates an $\hat{\mathbf{r}} \cdot \hat{\mathbf{n}}$ factor for detection on a planar surface. The instantaneous power incident on the detector is expected to be

$$\Phi(\mathbf{r}, t) \cdot d_x d_y \hat{\mathbf{n}} = d_x d_y L(x) \frac{P(t - t_b)}{4\pi r^2}. \quad (7)$$

The ballistic phonon signal (without quasiparticle absorption) for a sampling window between t_g and $t_g + \Delta t$ is predicted to be

$$I_b(x) \propto \int_{t_g}^{t_g + \Delta t} d_x d_y L(x) \frac{P(t - t_b)}{4\pi r^2} dt. \quad (8)$$

The experimental time trace shown in Fig. 8(a) gives us the function $P(t)$, which fits nicely to the empirical function $P(t) = Bt^2 e^{-t/\tau}$ by adjusting parameters B and τ . Finally, Fig. 8(b) shows the theoretical sound velocity $v(x)$ along a standard scan line needed to calculate $t_b = r/v(x)$ in the integral.

In Appendix B we show how the temporal shape of the source power function $P(t)$ affects the spatial distribution of transmitted phonons. A 4-mm crystal and short time gates ($\Delta t \ll \tau$) are used to obtain higher time and space resolution to confirm the validity of Eq. (8), which we now use for analysis of data from shorter samples with short time gates.

As in the previous analysis, the ballistic phonon intensity including quasiparticle absorption is

$$I(x) = I_b(x)[1 - A(x)], \quad (9)$$

where $A(x)$ is the usual absorbed fraction. Figure 9(a) shows a fit of this function to experimental transmission profiles for three relatively high excitation powers using w_b found in Sec. III for the Lorentzian width. Notice that the broad Lorentzian wings beyond ± 350 μm in the data of Fig. 5(b) for a long gate width ($\Delta t = 450$ ns) are totally flattened for the short gate width ($\Delta t = 50$ ns) used in the present experiment. The resulting absorption fractions A_o along $[110]$ are plotted as a function of temperature in Fig. 9(b) and fit to Eq. (5), using the value of α_n obtained in Sec. III. The power density varies by nearly two orders of magnitude for these three runs (yielding different $\beta\ell$) yet the resulting gap parameters Δ are consistently close to 1.3 meV. A semi-log plot in Fig. 9(c) shows that the absorption coefficients for these three data sets fall along a straight line with $\Delta = 1.31 \pm 0.08$ meV.

Finally, this general analysis is applied to the data presented in Paper I, which were taken at the highest excitation levels. Figures 10(a) and 10(b) show fits of Eq. (9) to typical spatial profiles for 1-mm and 2.5-mm samples, respectively. The slightly off-center alignment of the absorption dip may be due to a slight misalignment of symmetry axes in cutting the crystal. The agreement of the analysis with the data is very good.

The experimental $A_o(T)$ for the two crystals are plotted in Fig. 11(a), showing the largest fit values to $\beta\ell$ in our studies, but again the resulting equilibrium gaps are very close to the previous results in this paper. In Fig. 11(b) we plot the absorption constants $\alpha(T)$ together for the two crystals with *linear* axes, in order to compare to the empirical analysis of Fig. 13 in Paper I. Now the absorption coefficients for the two crystal thicknesses are in reasonable agreement.

The weak temperature dependences and anomalous path-length dependences found in the initial analysis of these crystals (Paper I, Fig. 13) are the result of a high number of nonequilibrium quasiparticles in the experiment. The present analysis shows that even at the highest temperatures (where equilibrium quasiparticle densities are highest) the nonequilibrium component outweighs the equilibrium component by the ratio 1.3: 1 for $L = 2.5$ mm and 3.1: 1 for $L = 1$ mm.

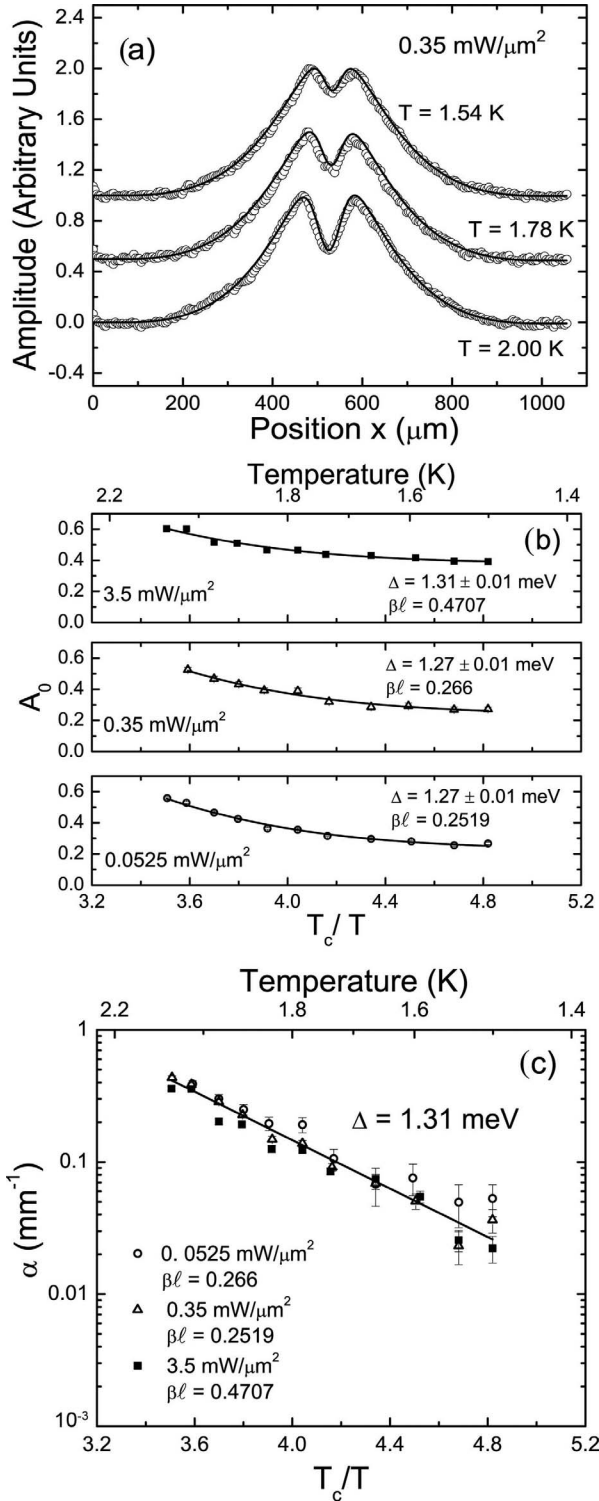


FIG. 9. (a) Transmission profiles for the 1.26-mm crystal excited by 10-ns pulses at medium peak power levels and sampled with a 50-ns gate. Solid curves are Eq. (9), using Eq. (8) for $I_b(x)$. (b) Absorbed fraction $A_0(T)$ for the three peak power densities shown. Solid curves are fits to Eq. (5) yielding the values of Δ and $\beta\ell$ shown. (c) Semi-log plot of the absorption coefficients $\alpha(T)$ showing good correspondence for the widely varying power densities. The straight line fit gives $\Delta = 1.31 \pm 0.08$ meV, in excellent agreement with the low power analysis in Sec. III.

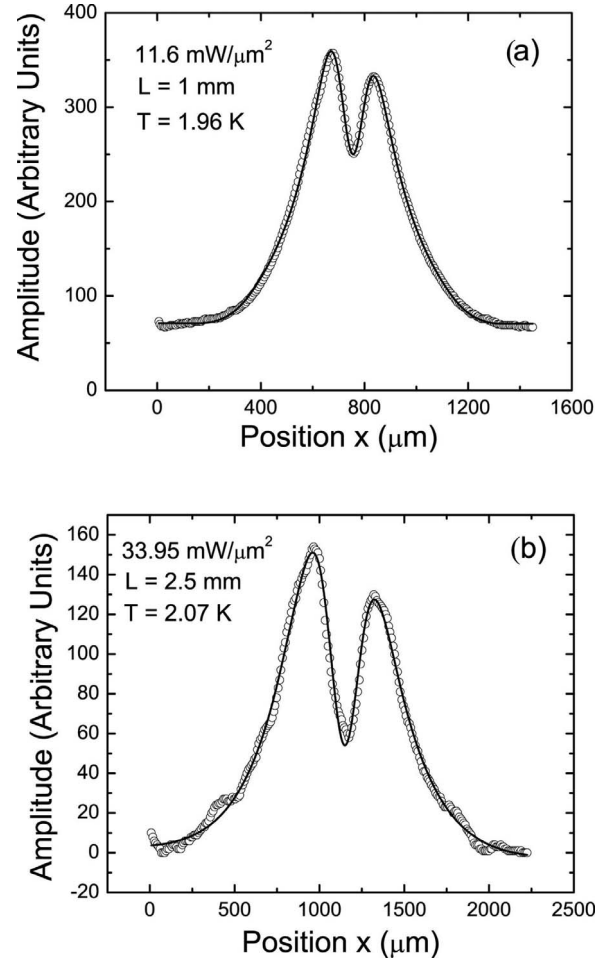


FIG. 10. Spatial profiles of the transmitted phonon signal for (a) 1-mm, and (b) 2.5-mm crystals at high excitation powers and using short boxcar gates, $\Delta t = 50$, and 200 ns, respectively.

V. TIME-INTEGRATED HIGH-POWER DISTRIBUTIONS AND $\beta\ell$ ANALYSIS

We conclude our discussion with an analysis of the equilibrium absorption coefficient obtained at relatively high excitation levels (high nonequilibrium quasiparticle densities), long path lengths ($L = 4$ mm), and long averaging time ($\Delta t = 1$ μ s). For short intense pulses, a new phenomenon appears, as shown in the time traces of Figs. 12(a) and 12(b), obtained with a 10 ns sampling time. In addition to the sharp LA and TA ballistic-phonon pulses, a broad underlying pulse is present. It is not simply due to phonons scattered from defects in the bulk of the crystal because the onset precedes the ballistic onset for LA phonons.

Indeed this new pulse is similar to that reported by Narayanamurti, *et al.*¹⁸ The broad signal was interpreted as a quasiparticle-phonon “heat pulse” propagating through the crystal. Basically, nonequilibrium quasiparticles recombine by emission of a high energy phonon that can create two new quasiparticles. This quasiparticle-phonon cloud dissipates only as the above-gap phonons down convert to subgap phonons. Moreover, because the ballistic velocities of quasiparticles are significantly greater than the sound velocity, a

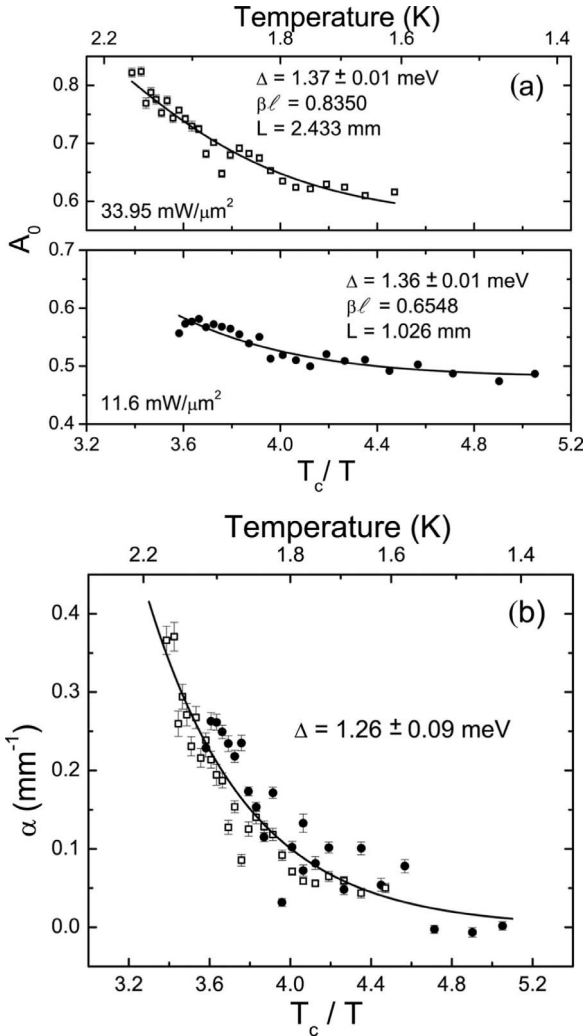


FIG. 11. (a) Absorbed fractions for 1-mm and 2.5-mm crystals and the theoretical fits with best-fit parameter values shown. Note that in this figure (unlike previous figures) we have expanded the vertical scale to better show the relatively small equilibrium contribution to A_o . (b) Absorption coefficients for the two crystals, plotted on a linear vertical scale in order to compare to the analysis of Paper I (Fig. 13) that did not account for nonequilibrium quasiparticles.

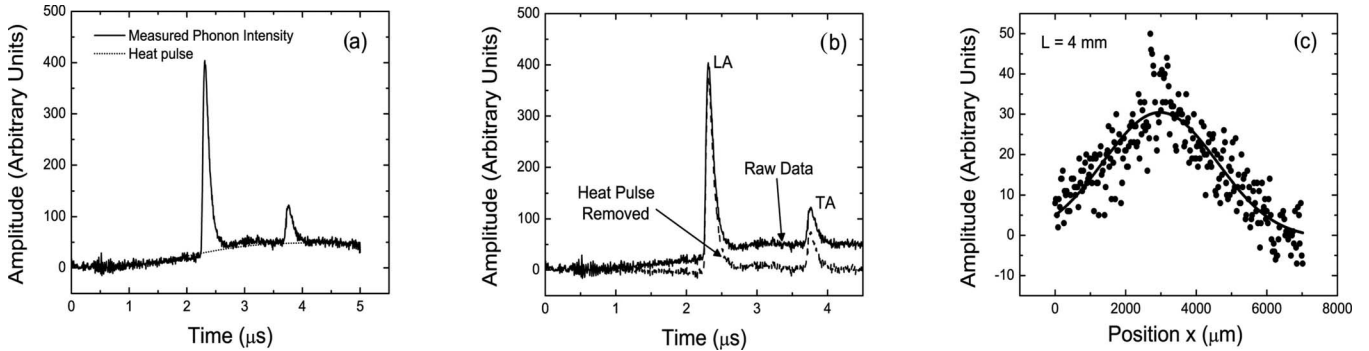


FIG. 12. (a) Time trace for a 4-mm crystal following a 10-ns excitation pulse with peak power density of 0.32 mW/ μm^2 . The sharp pulses are ballistic LA and TA phonons traveling along the [110] direction in Pb. A broad “heat pulse” with an onset at supersonic velocity lies under the ballistic components. (b) The effect of subtracting a function of the form $\text{erf}(t)e^{-t/\tau}$ representing the heat pulse from the total phonon signal. (c) Spatial profile of the heat pulse measured with a fixed 50-ns long boxcar gate starting approximately 50 ns before the LA ballistic pulse.

fraction of the diffusive “heat pulse” can have an effective velocity greater than the sound velocity.

For our purposes, it is necessary to include the spatial profile of the “heat pulse” in the analysis of the measured $I_{\text{tot}}(x) = I(x) + I_{hp}(x)$, where $I(x)$ represents the transmitted ballistic intensity of Eqs. (2)–(4), appropriate for a time-integrated (long-gate) measurement. The spatial profile $I_{hp}(x)$ due to the heat pulse is obtained by recording with a short boxcar gate the signal arriving just before the arrival of ballistic LA phonons. The result is shown in Fig. 12(c). The solid curve through the data is a Gaussian with a width, $\sigma_{hp} = 1.65$ mm, considerably broader than the width, $\sigma_s = 0.9$ mm, discussed in Appendix A for phonons scattered by isotopic defects. The dashed curve in Fig. 13(a) shows the contribution of the heat pulse profile to $I_{\text{tot}}(x)$ for the $T = 1.99$ K linescan.

The curves through the data in Fig. 13(a) are the function $I_{\text{tot}}(x)$, yielding the fractional absorptions $A_o(T)$, which are fit to Eq. (5) to yield the physical parameters $\beta\ell$ and Δ , as shown in Fig. 13(b). A semi-log plot of absorption coefficient $\alpha(T)$ for the two power densities is given in Fig. 13(c). Once again, the analysis yields a superconducting gap very close to the accepted gap for Pb. It is notable that if the “heat pulse” effect were not taken into account, the fitted absorption coefficients would be significantly larger and a smaller gap would be obtained.

Finally, we take a global view of all of our data concerning the generation of nonequilibrium quasiparticles. Recall that the factor $e^{-\beta\ell}$ represents the reduction in $I(x_o)/I_o$ due to nonequilibrium quasiparticles. This factor would include phonon absorption by nonequilibrium quasiparticles near heated excitation and detection surfaces, and possibly quasiparticles in a heat pulse. The $\beta\ell$ parameters derived from each of our fits to $A_o(T)$ are plotted in Fig. 14 as a function of peak power density (power per area) of the optical excitation.

We see that $\beta\ell$ increases in a monotonic fashion over the four-decade variation in power density. An empirical function $\beta\ell = 0.126 + 2.3P^{0.34}$ fits the data reasonably well. While we presently have no quantitative model for nonequilibrium quasiparticle generation in our experiments, it may be relevant that the temperature of a Planckian source varies as the fourth root of energy density. The value of $\beta\ell$ changes rather

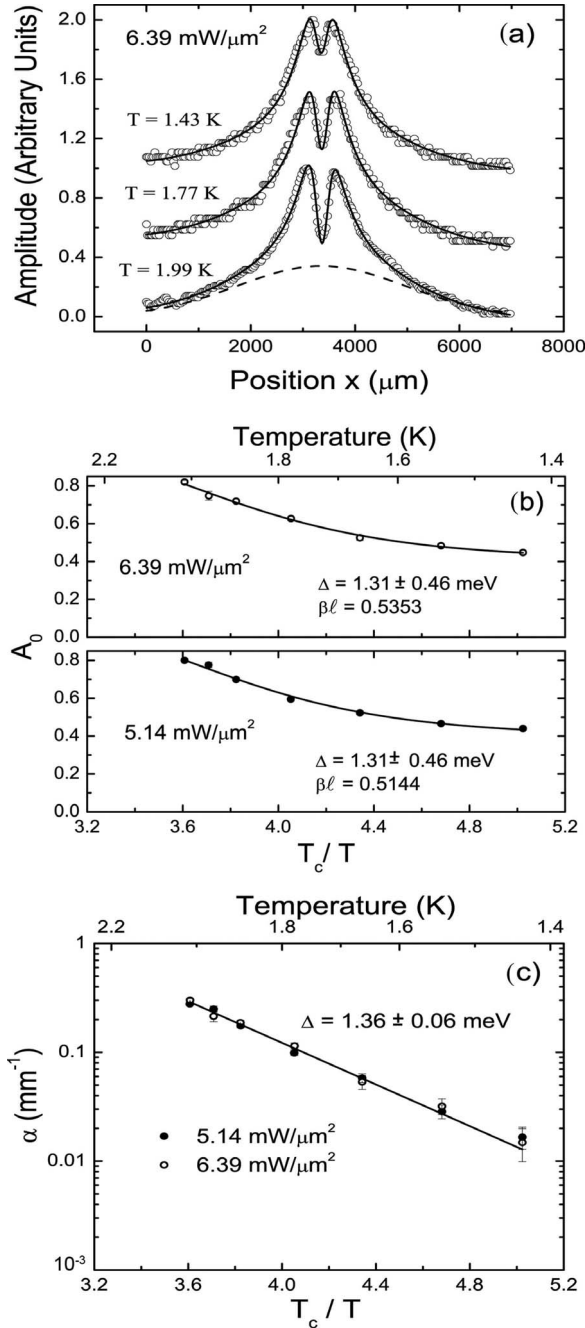


FIG. 13. (a) Spatial profiles at three temperatures for the time-integrated high-power-density experiments on the 4-mm crystal. The dashed line shows the ‘‘heat pulse’’ component as described in the text. (b) Fractional absorptions for two peak power densities. (c) Absorption coefficients $\alpha(T)$ for the two runs, showing good agreement with previous gap parameters.

slowly over the first two decades of power density and increases more rapidly over the second two decades. We suspect that the low-power limit is due to nonequilibrium quasiparticles generated by current biasing the detector. The temperature of this nonequilibrium quasiparticle source does not vary much from experiment to experiment. This situation would correspond to:

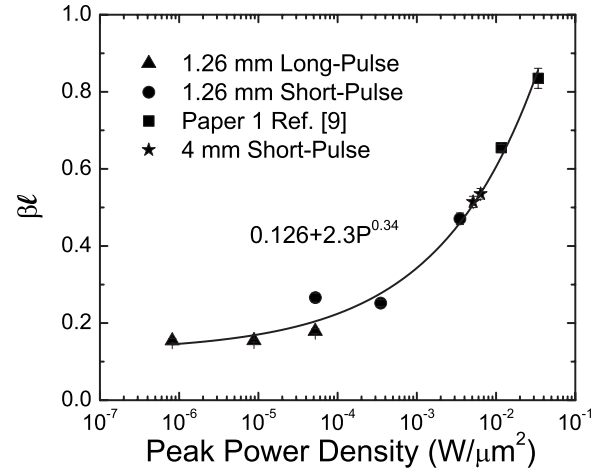


FIG. 14. Summary of the $\beta\ell$ parameters associated with non-equilibrium quasiparticles, including all of the data analyzed in this paper. Leveling off of $\beta\ell$ to a nonzero value for low power densities is likely due to excess quasiparticles created by warming the detector to its active temperature range.

$$\beta\ell = \beta_d \ell_d + \beta_e \ell_e, \quad (10)$$

where the first and second terms represent losses in ballistic phonons due to detector bias and excitation level, respectively. Complicating the description of source properties, studies⁹ have shown that for focused surface excitation, the thermal contact between sample and superfluid helium can be greatly reduced by the formation of a helium bubble, impairing the local cooling efficiency of the bath. Fortunately incorporation of a single parameter, $\beta\ell$, representing the total number of nonequilibrium quasiparticles in the path of ballistic phonons, enables us to extract equilibrium properties in the bulk of the sample.

VI. SUMMARY AND CONCLUSIONS

We have employed ballistic phonons to probe the densities of quasiparticles in a superconducting Pb crystal. As shown in the accompanying paper,⁷ the anisotropic Fermi surface of Pb leads to a sharp angular distribution of phonons that interact strongly with quasiparticles. The initial experiments were successful in showing diminishing phonon absorption as the crystal temperature was lowered, but the magnitude and temperature dependence of the absorption coefficient changed with sample length. These anomalous effects were not explained by a theory incorporating scattering of phonons from isotopic defects in the bulk. An experiment with a low-pass phonon filter led us to consider the possible effects of nonequilibrium quasiparticles generated by the phonon-imaging technique.

Our first step in the present work was to develop a theoretical basis for analyzing the experimental data. Monte Carlo simulations of ballistic and scattered phonons, employing the full elastic anisotropies in the crystal, provided time-integrated transmission functions. A straightforward theoretical approach including effects of the temporal distributions of ballistic phonons allowed us to extend the calculations to

experiments resolved in time and space. The data and analyses for a wide variety of experiments all led to the same conclusion: The equilibrium quasiparticle density in high-purity Pb is consistent with the generally accepted BCS temperature dependence and provides a zero-temperature gap parameter averaged over all our data sets, $\Delta = 1.32 \pm 0.07$ meV, consistent with electron tunneling data.

In short, we have found no evidence for the highly anisotropic gap that was predicted from considerations of an SDW electronic ground state. Using our lowest experimental temperature of 1.45 K and measured gap parameter $\Delta = 1.32$ meV, the BCS exponent for Pb has decreased to the value $\exp(-\Delta/k_B T) = 2.6 \times 10^{-5}$. Ballistic phonons have provided an uncommon yet powerful bulk probe of superconductivity in this crystal.

ACKNOWLEDGMENTS

This work was supported in part by the U.S. Department of Energy, Division of Materials Sciences under Grant No. DEFG02-96ER45439, through the Frederick Seitz Materials Research Laboratory at the University of Illinois at Urbana-Champaign.

APPENDIX A: SIMULATION OF PHONON SCATTERING FROM ISOTOPIC MASS DEFECTS

In this addendum we consider how phonons scattered from mass defects in the bulk of the sample could affect the observed transmission profiles. A realistic scattering model must include acoustic anisotropies and mode conversion between phonons of different polarization.⁹ We have incorporated these factors plus the dependence of elastic scattering rate on phonon frequency in a Monte Carlo simulation, assuming an initial Planckian distribution at temperature T_s and the measured elastic parameters and density of Pb.

For $T_s = 20$ K a standard line scan through the distribution of scattered phonons arriving at the detection surface ($L = 4$ mm) is shown in Fig. 15(a). The collection time for this scan is $\Delta t = 1 \mu\text{s}$ corresponding to the experimental conditions for data taken in the 4-mm sample. The solid curve, a Gaussian function with $\sigma_s = 927.72 \mu\text{m}$, provides a reasonable fit to the data. Corresponding profiles for different source temperatures are given in Fig. 15(b), showing that the distributions do not change significantly as the source temperature is raised above 20 K, but they level off in amplitude at a value approximately 10% of the ballistic amplitude in the [110] direction. In part, this result is due to the fact that phonons with frequencies above $2\Delta_o/h = 650$ GHz easily break Cooper pairs and are not transmitted through the sample. Another reason that the distributions remain constant with increasing source temperature is that higher frequency phonons scatter more often than the lower frequency phonons associated with cooler sources. The extra scattering events produce phonons that arrive after the $1 \mu\text{s}$ collection gate.

As discussed in Sec. III, the low power time-integrated spatial profiles for a 1.26-mm sample are well explained by phonons that travel ballistically from source to detector, us-

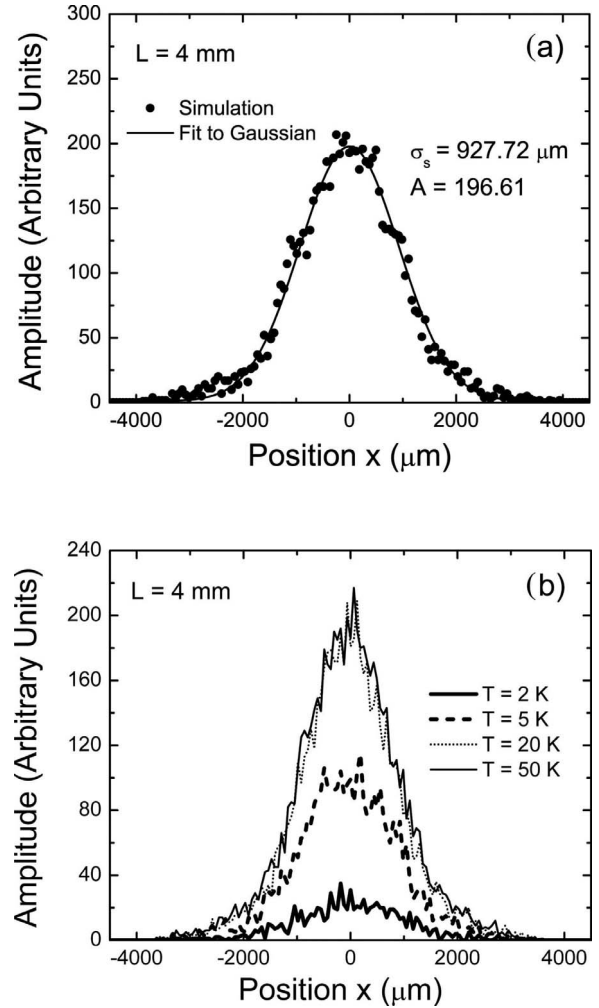


FIG. 15. (a) Standard scan line through a distribution of phonons emanating from a 50-K Planckian phonon source, which are scattered by isotopic defects and arrive at the detection surface less than $1 \mu\text{s}$ after the ballistic arrival time. (b) Distribution of scattering events along the same line as in (a) for several source temperatures.

ing Eq. (5). Including the somewhat broader Gaussian scattered component in the fitting routine results in zero amplitude for the scattering profile. There are several factors that contribute to the absence of scattered phonons in these data. When an LA phonon scatters from a defect, it is highly likely to convert to a TA phonon due to the much larger density of TA states. Since the TA-mode velocity is a factor of two or more, slower than the LA mode, most of these phonons do not arrive in time to be counted in the collection gate. The polarization selection rules also favor LA phonons scattering at near right angles to their original direction. Essentially, not many scattered phonons arrive at the detection surface within the selected time window Δt . This is especially true for short gates and samples of thickness less than about 2 mm.

APPENDIX B: TESTING THE SHORT-GATE THEORY AT HIGH ANGULAR RESOLUTION

Equation (8) is a basic description of phonons emitted from a finite-lifetime point source and arriving at a detection

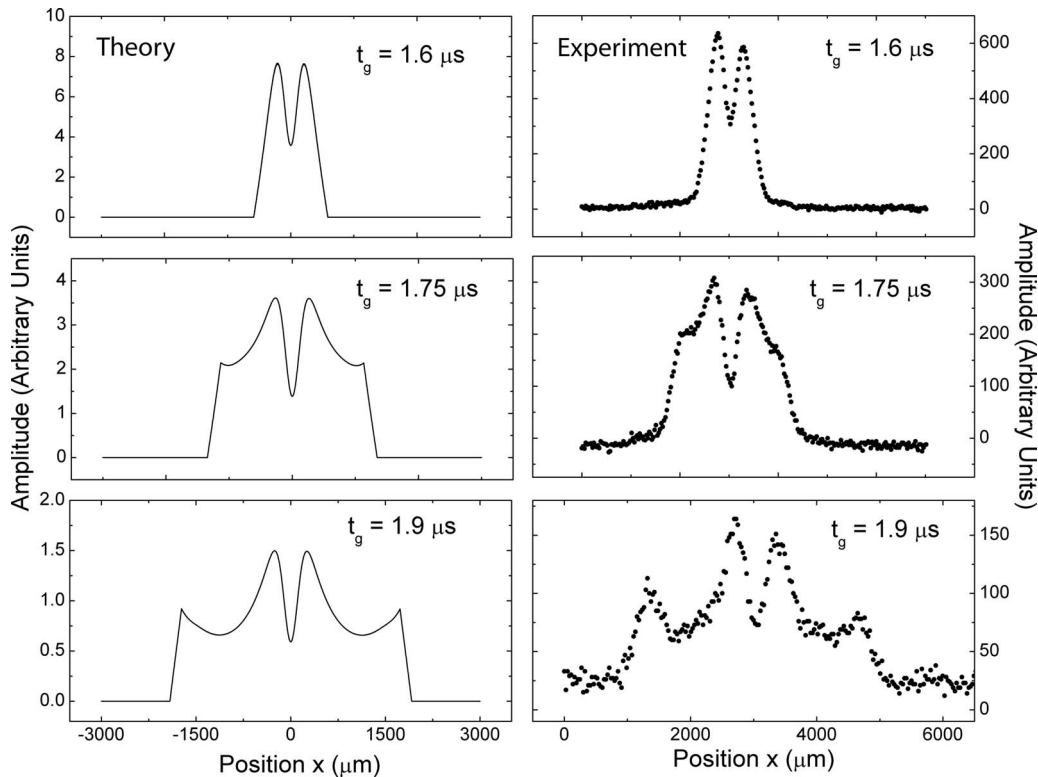


FIG. 16. Time-resolved spatial profiles of phonon transmission at a high power and high angular resolution ($L=4$ mm). The right column is data measured in a 4-mm sample, and the left column shows the line scans predicted by Eq. (8) for the same gate-start times as the data.

surface. It assumes that all phonons travel ballistically (without scattering in the crystal) and that the arrival pulse $P(t-r/v)$ is just a retarded replica of the emission power $P(t)$. The experiment corresponding to Eq. (8) in Sec. IV used a crystal with 1.26-mm thickness and a 50-ns gate width, and those spatial profiles dropped quickly to zero for increasing x . The effect of $P(t)$ in Eq. (8) can be shown more clearly by performing a similar experiment with a crystal of 4-mm thickness, which allows three times higher angular resolution of the detected profile and more temporal separation between LA and TA arrival times.

The results are shown in Fig. 16. The function resembling the arrival pulse, $P(t-r/v)$, is similar to that shown in Fig. 8(a). This function is used in Eq. (8) to calculate the spatial profiles of transmitted phonons as the start time (t_g) of a 50-ns wide gate is delayed. Calculated profiles at three delay

times are shown at the left, and the corresponding experimental data are presented at the right.

At $t_g=1.6$ μ s, the boxcar samples a 50-ns window between 1.6 and 1.65 μ s that is close to the ballistic arrival time for LA phonons traveling along [110]. At increasing t_g the boxcar is sensitive to phonons arriving at larger path lengths r , corresponding to signals at larger $x=(r^2-L^2)^{1/2}$. The central part of the spatial distribution, however, remains as indicated by the Lorentzian profile with a Gaussian absorption dip. The finite-lifetime source produces a significant number of phonons whose delayed arrival time along [110] contribute (albeit weakly) to the center region of the distribution. The agreement between theory and our high-resolution data show that the assumptions behind Eq. (8) are quite valid and that this straightforward theory is applicable to the experiments reported in Sec. IV.

*Present address: Physics Department, Abilene Christian University, Abilene, Texas 79699, USA.

¹E. Fawcett, *Rev. Mod. Phys.* **60**, 209 (1988).

²A. W. Overhauser, *Phys. Rev. Lett.* **4**, 462 (1960).

³L. L. Daemen and A. W. Overhauser, *Phys. Rev. B* **39**, 6431 (1989).

⁴A. W. Overhauser and L. L. Daemen, *Phys. Rev. Lett.* **61**, 1885 (1988).

⁵B. J. C. van der Hoeven, Jr. and P. Keesom, *Phys. Rev.* **137**,

A103 (1965).

⁶P. H. Keesom and B. J. C. van der Hoeven, Jr., *Phys. Lett.* **3**, 360 (1963).

⁷J. D. Short, T. L. Head, and J. P. Wolfe, preceding paper, *Phys. Rev. B* **78**, 054515 (2008).

⁸A. W. Overhauser and T. M. Giebultowicz, *Phys. Rev. B* **47**, 14338 (1993).

⁹J. P. Wolfe, *Imaging Phonons: Acoustic Wave Propagation in Solids* (Cambridge University Press, Cambridge, 1998).

- ¹⁰For all experiments in Paper I (Ref. 7) excepting the phonon-filter experiment, an SiO film is deposited between a Cu excitation film and the Pb crystal. In all the experiments described in this paper (and the phonon-filter experiment), we use an Au excitation film deposited directly onto the crystal. As shown in Secs. III and IV, both excitation-film configurations yielded consistent results in determining the superconducting gap. The Cu/SiO film did show longer source lifetimes at higher powers, and the single Au film produced more of a “heat pulse” described in Sec. V and Ref. 18.
- ¹¹The Au was found to adhere better than Cu over SiO used for the 1 and 2.5-mm samples in Paper I. A directly deposited metal excitation film does produce some differences in the temporal behavior of the phonon source, but our principal results are not affected by the choice of excitation film.
- ¹²M. Tinkham, *Introduction to Superconductivity* (McGraw-Hill, New York, 1998).
- ¹³B. R. Tittmann and H. E. Bömmel, Phys. Rev. **151**, 178 (1966).
- ¹⁴N. W. Ashcroft and N. D. Mermin, *Solid State Physics* (Saunders, Philadelphia, 1976).
- ¹⁵More recent tunneling studies show that the gap is actually multivalued and slightly anisotropic. See the beginning of Sec. IV in Paper I. We quote 1.35 meV as a representative value.
- ¹⁶N. E. Phillips, M. H. Lambert, and W. R. Gardner, Rev. Mod. Phys. **36**, 131 (1964).
- ¹⁷We note however that a T^2 dependence of specific heat is expected for mobile dislocations. See Ref. 19.
- ¹⁸V. Narayanamurti, R. C. Dynes, P. Hu, H. Smith, and W. F. Brinkman, Phys. Rev. B **18**, 6041 (1978).
- ¹⁹A. Granato, Phys. Rev. **111**, 740 (1958).